Deceleration and Confinement of Accelerated Ions

Öztürk S. B., Yedierler B.

Middle East Technical University, Çankaya, Üniversiteler St., TR

E-mail: `berkay.ozturk_01@metu.edu.tr, buraky@metu.edu.tr`

03.09.2022

Abstract. We present a project that is a promising solution to the transportation problem of lunar mined materials such as He-3 isotope, to be used on the earth. It is proposed that, using the linear accelerator technology, the coals mined on the lunar surface may be transferred to a satellite orbiting the moon, similar to the Capstone satellite orbit of NASA. The satellite has ion decelerating electrostatic rings to decelerate the received ion beams and plasma confinement machine to confine the injected ions. We simulated the ion trajectory passing through the deceleration electrostatic rings in python environment. It is determined that the ion is decelerated successfully with the optimized charge density for the electrostatic rings. After the deceleration simulation, confinement simulation is done and it is concluded that the ions are successfully confined in the proposed plasma confinement machine, even though plasma-wall interactions may occur.

1. Introduction:

Harnessing the power of the sun, that is created in a laboratory. Fusion power has been one of the most promising solution to rising global temperatures and increasing energy demands. For decades, scientists have been studying the ways of achieving fusion power by understanding the behavior of the plasma [1] [2]. To be precise, fusion reaction has already been achieved. However, the aim is to get a net gain factor above 1, where the gain factor measures the ratio between given energy versus produced energy during the fusion reaction [3]. We are concentrating on an element that is considered to be more efficient than currently preferred elements, Deuterium-Tritium for fusion reaction. In 1988, a NASA report states that even though D/T fusion is more near term, D/He-3 may be the best option for commercial purposes [4]. The problem with He-3 is that it is a rare gas element in the earth that can only be produced artificially in small amounts by several methods [5]. Therefore, the only option seems to be mining the moon which is rich in terms of He-3 isotope, and it is already a competitive area among many engineers, scientists, and governments [6] [7] [8]. In this project, we are aiming to eliminate the interplanetary transportation problem of the mined coals from other planets. With conventional methods, the mined coals are gathered to the earth by rockets, which is expensive and not profitable. Therefore, we propose a new transportation technique for

He-3 isotope or any other mined material. The mined substances are accelerated using linear particle accelerators from the moon or other planets and are received by a satellite orbiting around the earth. The accelerators are widely used in particle physics projects and widely investigated [9][10][11]. Also, the confinement methods are studied in the fusion research, and necessary expertise has developed throughout the last century [12]. This research covers the deceleration and confinement of ions that have been accelerated and excludes the acceleration of substances that are being mined. To decelerate the ions, a set of aligned electrostatic rings [13][14], and to confine the decelerated ions, magnetic mirror geometry is chosen [15]. We plan to optimize the parameters for deceleration and confinement using single particle kinematics of ion optics and plasma physics. After the analytical solution is gathered and deceleration/confinement parameters are optimized, the trajectory is going to be simulated and analyzed using several libraries in python.

2. Ion Deceleration Instrument & Calculations

2.1. Configuration of the Instrument

The configuration is composed of four sequential electrostatic rings with a ring radius of 0.05 meters, and the spacing between the rings 0.15 meters, which is close to the real experimental system to be constructed. As the particle passes through each ring, the particle is aimed to be decelerated from 1e6 m/s until the final velocity of 5e1 m/s. The configuration of the multiple ring system is plotted in ANSYS MAXWELL, and shown in figure 1. In order not to re-accelerate the passing beam, electrostatic rings are embedded in and placed near the ends of the faraday cages with a distance of smaller than $r/\sqrt{2}$, which is the maximum electric field at the distance, where r is the radius of the electrostatic ring.
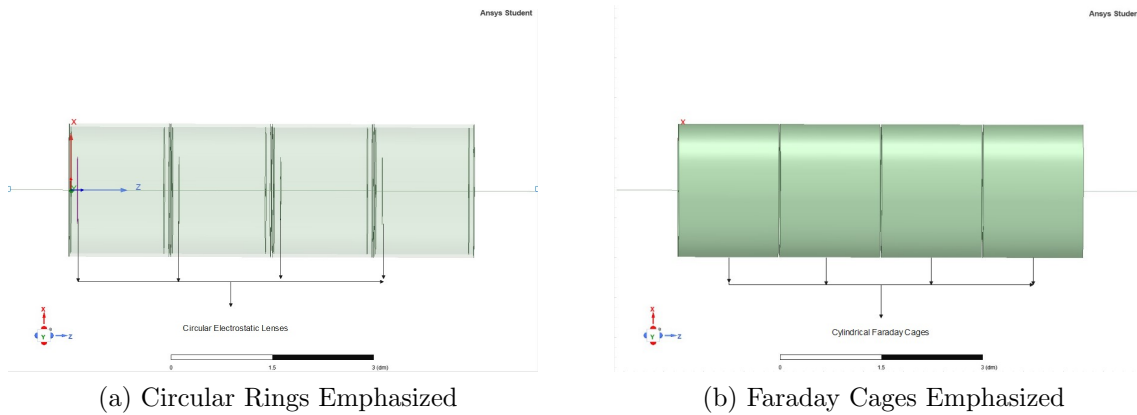

(a) Circular Rings Emphasized   (b) Faraday Cages Emphasized

Figure 1: Showing electrostatic rings embedded in faraday cages.

2.2. Optimizing the Charge Density

In order to acquire the required charge density of the deceleration rings, the ion beam radius is considered to be small and moving along the axis. Therefore, the electric field of the electrostatic ring along the z-axis is taken into account.

Where the electric field of a uniformly charged ring is given by,

$$\vec{E} = \frac{\lambda r z}{2\epsilon_0 (r^2 + z^2)^{\frac{3}{2}}} \hat{z} \tag{1}$$

Since the electrostatic rings are not in free space but in faraday cages, there are harmonics that are determined by the separation of variables. The basic configuration is shown in the figure below, and the solution gathered by solving the Laplace problem in Cartesian coordinates is given as equation 2
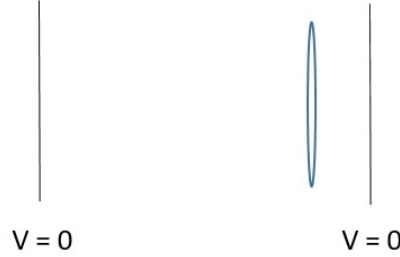

V = 0   V = 0

Figure 2: The configuration of the electrostatic ring in a single faraday cage.

$$E_{cage} = \sin(\frac{3\pi z}{2a}).E_{ring} \tag{2}$$

Where, a is the length of a cage.

Using the energy loss due to the electric field, the desired line charge density may be acquired. Where electric potential energy and the evaluated work done on the projectile ion is,

$$U = -Q_p \int_0^a E dz \tag{3}$$

$$W_e = KE_i - KE_f = \frac{1}{2}m_p(v_i^2 - v_f^2) \tag{4}$$

We can get the charge density using the energy conservation and leaving the charge density alone, where the result is shown in Eq. 5,

$$\lambda = \frac{\epsilon_0}{Q_p r}m_p(v_i^2 - v_f^2) \left(\int_0^a \sin(\frac{3\pi z}{2a}) \frac{z}{(r^2 + z^2)^{\frac{3}{2}}} dz \right)^{-1} \tag{5}$$

The integral is evaluated using numerical methods, scipy quad integration library. The numerical result is 9.51 with 5 10^{-10} error value.

2.3. Field Simulation Using Finite Element Method

The field simulations are done using ANSYS Maxwell. The charge densities are set as the same as in the numerical calculations, the positions and total charge that the rings carry are given in table 1.

Table 1: Properties of the decelerating electrostatic rings.

Ring Number	Charge [C]	Charge Density [C/m]	Position [dm]	Velocity After Pass [m/s]
1	$3.30 \ 10^{-8}$	$1.05 \ 10^{-7}$	0	$8.0 \ 10^5$
2	$4.39 \ 10^{-8}$	$1.40 \ 10^{-7}$	1.5	$4.0 \ 10^5$
3	$1.41 \ 10^{-8}$	$4.48 \ 10^{-8}$	3.0	$8.0 \ 10^4$
4	$5.86 \ 10^{-10}$	$1.87 \ 10^{-9}$	4.5	$1.0 \ 10^2$

To gather the best result, curvilinear meshing is applied as the surface of all the objects is curved. The vector field outside the cages is given in figure 3. As can be seen from figure 4a, no fields reach outside the faraday cages, as expected. Also, the electric field data comparison with the numerical calculation that has been shown in figure 4.
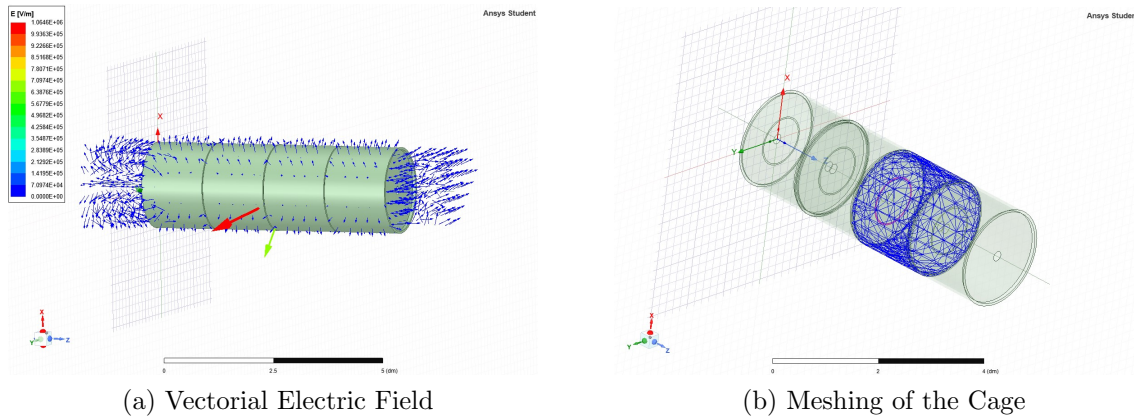

(a) Vectorial Electric Field

(b) Meshing of the Cage

Figure 3: a) Showing the vector fields outside the faraday cage, b) showing the configuration and meshing of the system.

2.4. Comparison of Generated Electric Fields

The generated electric field in ANSYS Maxwell by finite element method and numerical calculation in python are compared in the following figure. It is seen that high order harmonics may be included in the numerical calculation to get the best result. On the other hand, the difference in the field data may be due to the stiffness of the electric field function and the convergence problem. Since the electric field of the electrostatic ring having a small radius is a stiff problem, the program needs a high number of passes to get a converging data.
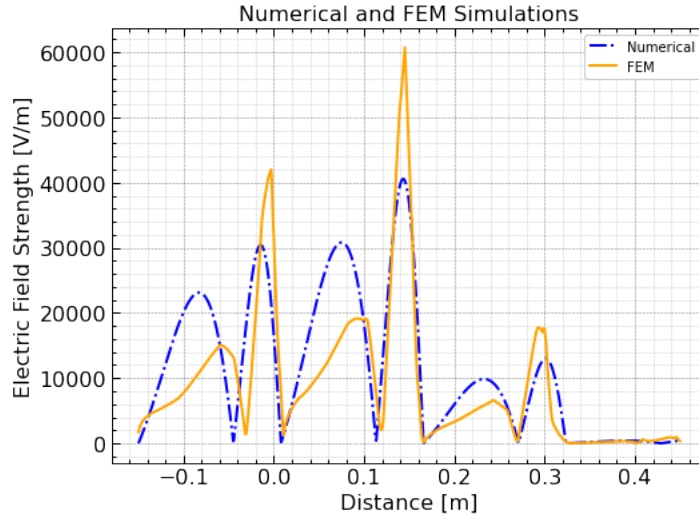
Figure 4: Comparison of generated electric fields, dashed blue lines representing numerical result, orange lines representing FEM result.

2.5. Particle Trajectory Simulation

Setting the initial velocity 1e6 [m/s], and the final desired velocity as 1e2 [m/s], with projectile charge 3.2e-19 Coluomb and mass of 3 amu (for the Helium-3 isotope), the required line charge density is found as in Table 1. As a differential equation solver, solve_ivp[16] of scipy module in python is preferred. Even though it is slower than the "Odeint" module, it gives freedom of determining relative tolerance (rtol) and absolute tolerance (atol), which is crucial in such stiff systems. While determining the method to be used, the methods that are specialized for stiff systems called LSODA and BDF embedded within scipy module have been tried. However, LSODA and BDF methods did not converge to the expected value. Therefore, DOP538 method that is used in chaotic systems with Runge-Kutta of order 8 solver is preferred and resulted in an expected value with considerable error.

To gather the solution, the equations of motions are given as follows,

$$\frac{d\vec{x}}{dt} = \vec{v} \tag{6}$$

$$\frac{d\vec{v}}{dt} = \vec{E} \, \frac{Q_p}{m_p} \tag{7}$$

Eventually, with the initial position of 0.15 meters, and an initial velocity of 1e6 m/s, the simulation is done. The result is given in the figures 5.

2.6. Error Analysis of the Trajectory Simulation

The expected final velocity was 100 m/s, however, the acquired final velocity was 140 m/s. The error is most likely produced by high number of steps with small step
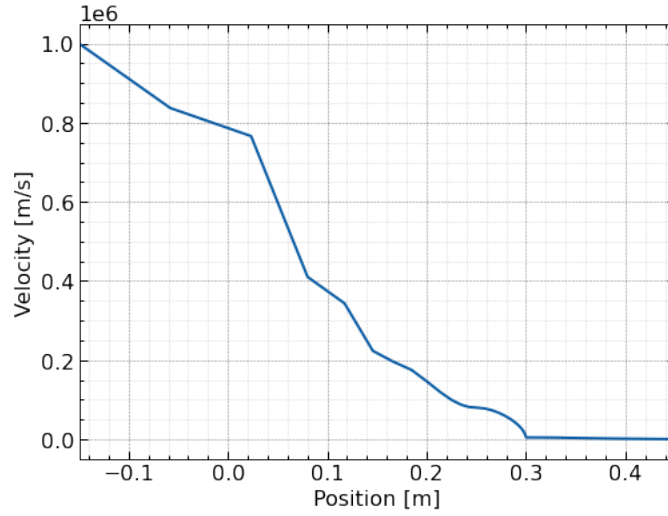
Figure 5: Position vs Velocity graph, illustrating the deceleration of the ion passing through deceleration rings.

size, which is 1e-7 seconds. As the steps taken in the ODE increase, each local error contributes to the global error, where the local error in Runge-Kutta of order 8 is $O(h^8)$, the global error is $O(h^7)$. According to research by R. England[17], the results lies in the error margin.

3. Ion Confinement Instrument & Calculations

3.1. Configuration of the Instrument

Magnetic mirror geometry is set as 3-3 with circular steady current line, symmetric with respect to the origin. The fields are produced from these rings with 1000 points each, and calculated using the Biot-Savart Law in python environment. The configuration is replicated in ANSYS Maxwell with the same current values, and the physical values corresponding to the current lines may be found in the table 2. The configuration and the magnetic field strength on z axis in both simulations may be found in the figures below.

3.2. Determination of Currents & Injection Angle

In order for the particle to stay within the configuration, it should constantly be following the guiding magnetic field lines. Therefore, the Larmor radius must not be larger than length scale of the system, as the particle would escape. Where the larmor radius is $r_l = v/w_c < 1$, and the gyro frequency of the particle is $w_c = Q_p B/m$. Considering that, $Q_p B/m = 10^5 B \approx 10^{-2} I$, the condition for the current rougly is $|I| > 100|v|$, in Amperes. Note that, $Q_p \approx 10^{-19} C$, $m \approx 10^{-24} g$, and the length scale is held unity

On the other hand, for a projectile with angle penetrating from the center of the z axis, the confinement angle is given as $\sin^2 \theta_m = B_0/B_m$, where B_0 is the field strength at $r = (0, 0, 0,)$, and B_m is the field strength at $r = (0, 0, a_z)$, where a_z is the turning point for the particle. With $a_z = \pm 2.05$, $B_0 = 0.3410^{-7}$, and $B_m = 5.1210-6$, the confinement angle is found to be $\theta_m = 25.27°$. Particles injected less than the confinement angle are inside the loss cone and can't be confined inside the magnetic mirror.

Table 2: Properties of the current lines.

Ring Number	Z Position [m]	Radius [m]	Current [A]
1	1	3	0.5
2	2	2	0.5
3	2.5	1	10
4	-1	3	0.5
5	-2	2	0.5
6	-2.5	1	10

3.3. Particle Trajectory Simulation

As a partial differential equation solver, solve_ivp module of scipy library is preferred, as is used in the deceleration simulation. With a duration of 20 seconds and 5e3 time steps, the following equations were solved.

$$\frac{d\vec{x}}{dt} = \vec{v} \tag{8}$$

$$\frac{d\vec{v}}{dt} = \frac{Q_p}{m_p}(\vec{v} \times \vec{B}) \tag{9}$$

Where initial velocity is,

$$\vec{v} = (20 \sin \theta_m/\sqrt{2}, \ 20 \sin \theta_m/\sqrt{2}, \ 20 \cos \theta_m) \tag{10}$$

With $|\vec{v}| = 20 \ m/s$

Eventually, the simulation is run for about 15 minutes, and the solution is gathered with 1e-7 rtol and 1e-9 atol. The particle is found to be successfully confined with the determined parameters. Energy conservation during the confinement simulation is shown in figure 7, illustrating no work is done with magnetic field. The position and velocity magnitudes of different axes are given in figure 8, and the general particle trajectory is given in figure 9.

(a) Configuration in ANSYS Maxwell

(b) Configuration in Python
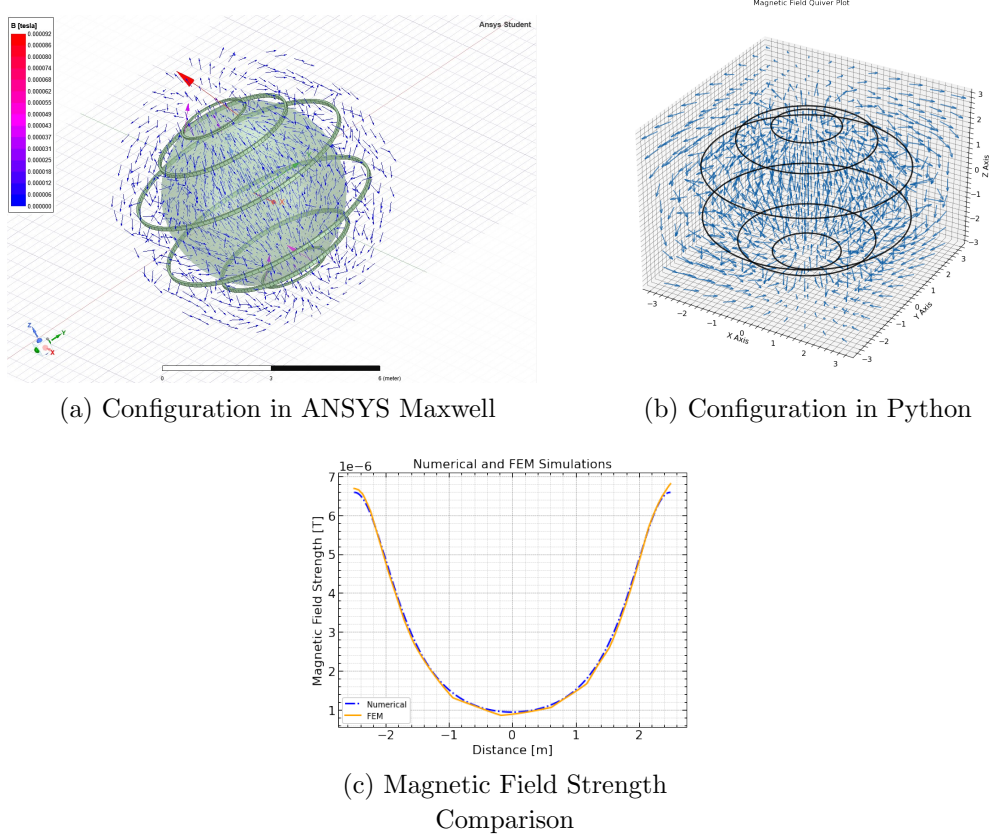

(c) Magnetic Field Strength
Comparison

Figure 6: : The configuration is illustrated in the figures on top where the currents run on the azimuthal axis and field lines are shown with the quiver plot. The magnetic field strength along the z-axis illustration on the bottom figure, blue dashed lines for the calculated values in python, orange line for values calculated in ANSYS Maxwell
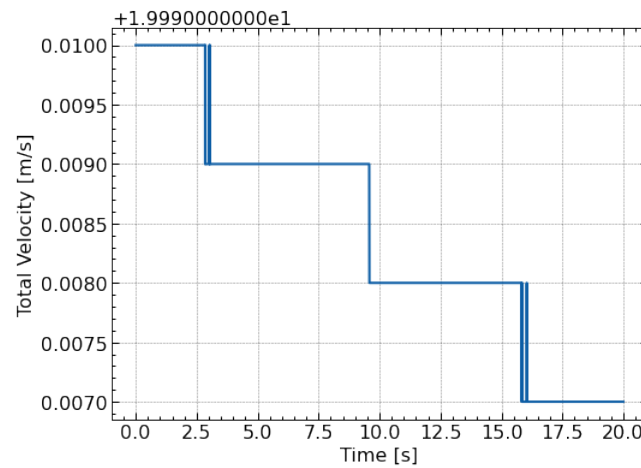

Figure 7: The configuration of the electrostatic ring in a single faraday cage.
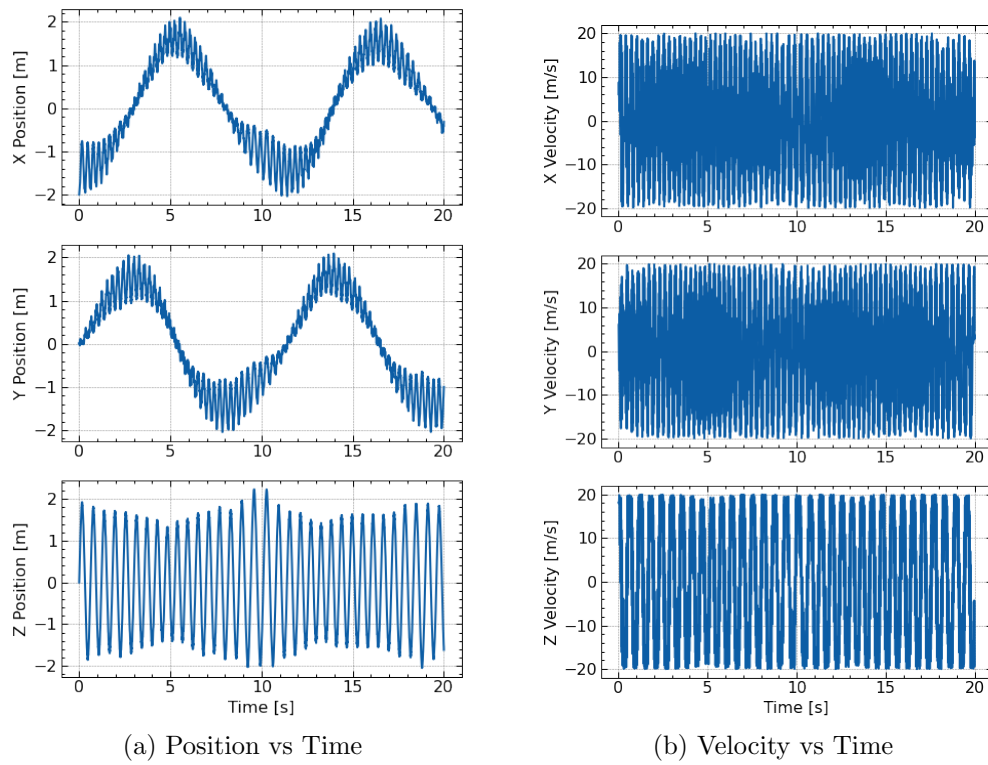
(a) Position vs Time

(b) Velocity vs Time

Figure 8: Position vs. Time and Velocity vs. Time graphs for different axes.
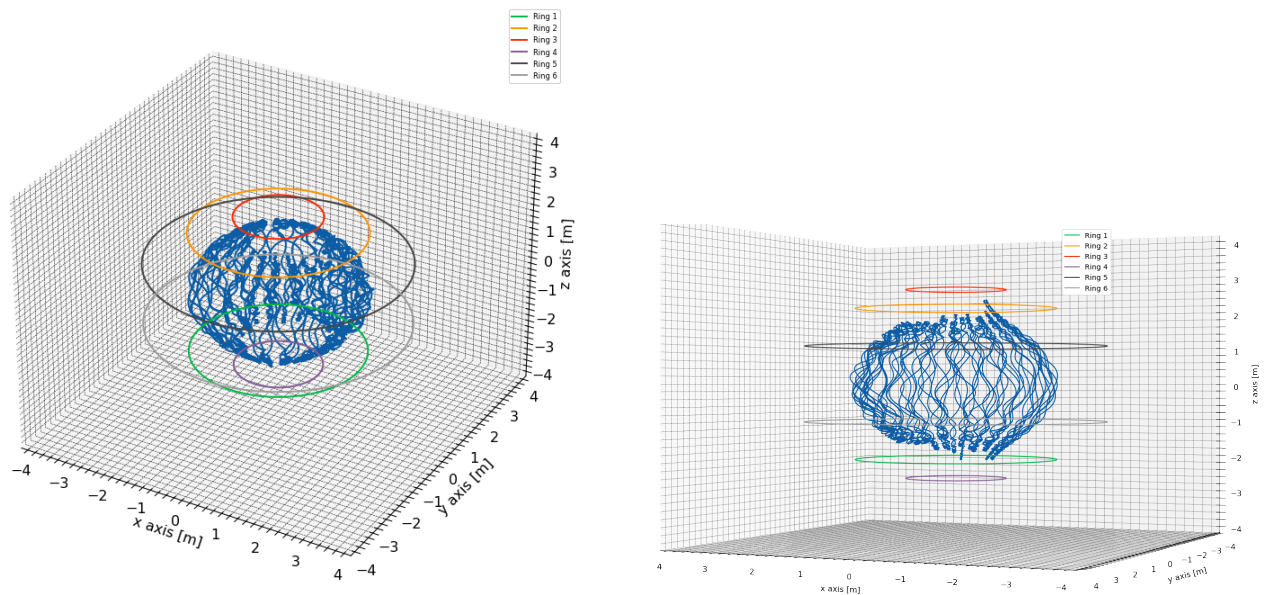

Figure 9: 3D Particle trajectory with different sight angles.

4. MHD Analysis

4.1. Motivation

Even though it is shown that particles are confined successfully with single particle trajectory simulation, in a dense and self-interacting plasma, it is crucial to investigate equilibrium conditions using Magnetohydrodynamics (MHD) theory or Kinetic Theory of Plasmas to find if plasma expansion occurs which results in escape of the particles. Furthermore, it is known that due to collisions in the dense plasma, particles change their direction which leads them to get into the loss cone.

4.2. Plasma Behavior Analysis

To make sure that we can use MHD theory, it is crucial to extract S-Parameter, which determines whether the plasma behavior is determined by MHD Theory or by Kinetic Theory [18][19]. Where the condition for kinetic motion to be dominant in plasma motion is,

$$S = \frac{r/2}{< r_c >} \leq 2 \tag{11}$$

Where, $S \equiv$ S-Parameter, $r \equiv$ Radial thickness of the configuration, $< r_c > \equiv$ Average larmor radius.

To extract the resultant S-Parameter, the particle trajectory simulation in spherical magnetic mirror (Spherical Pinch) is replicated with injection angle of $\theta = 71.8$, and the other simulation parameters are equivalent to the first simulation, as described in the particle trajectory simulation section. The simulation diagnostics may be found in figrue 10.
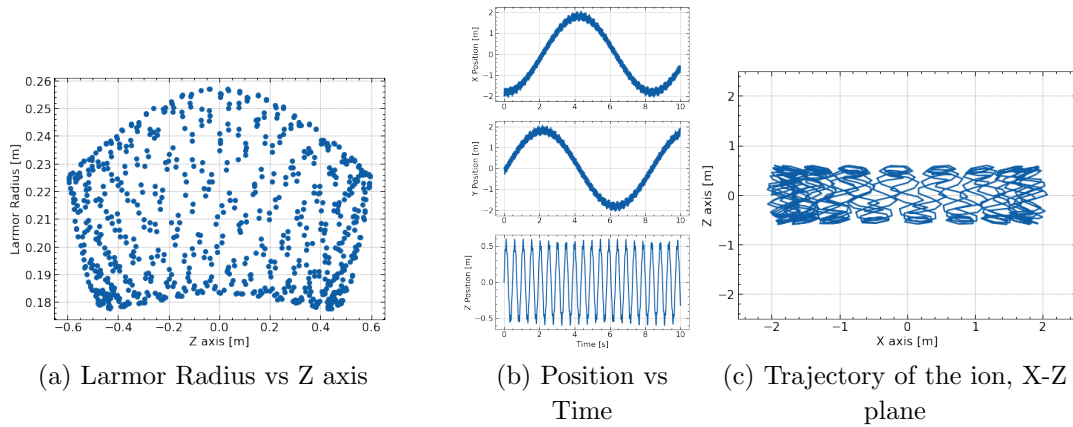

(a) Larmor Radius vs Z axis   (b) Position vs Time   (c) Trajectory of the ion, X-Z plane

Figure 10: Plasma diagnostics results for the ion confinement simulation with $\theta = 71.8$ injection angle.

The resultant average larmor radius is 0.209 meters, the thickness of plasma is 2.07 meters, and the resultant s-parameter is 4.94. Which implies that the plasma behaves like fluid and not ruled by kinetic effects, according to finite larmor radius effect. At higher particle speeds, S-Parameter grows even more, due to increasing magnetic field and decreasing average larmor radius.

4.3. Particle Distribution Model

The MHD model considers the plasma as a fluid. In a confinement machine, the plasma is held inside with applied magnetic pressure. Therefore, if the plasma is in its equilibrium state where no expansion occurs, it is considered that the total pressure vanishes near the plasma confinement boundaries. Hence, pressure distribution may be modeled by the mass distribution of the plasma. The general fluid pressure is described by the equation 12.

$$P_{(r)} = P_0 \left(\frac{\rho_{(r)}}{\rho_0} \right)^{\gamma} \tag{12}$$

Where, $P_0 \equiv$ Average pressure, $\gamma \equiv$ Polytropic index, $\rho_0 \equiv$ Average mass, $\rho_{(r)} \equiv$ Radial mass distribution.

Henceforth, estimating the mass distribution from the particle trajectory, we may gather how the system evolves. According to the figure 15, particles follow an unduloid-like pattern. However, since a closed surface estimation is needed to replicate confinement, spheroid geometry is preferred. The explicit solution is given by equation 13, and the geometry of spheroid is given by figure 11.
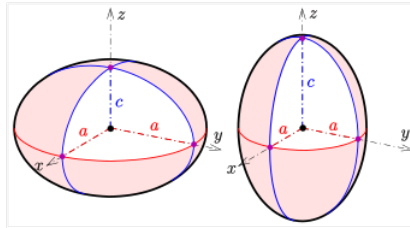

Figure 11: Showing the spheroid geometry, oblate on the left, prolate on the right.

$$\frac{x^2 + y^2}{a^2} + \frac{z^2}{c^2} = 1 \tag{13}$$

Now, we estimated the general curvature of the fluid. To estimate the distribution around the spheroid curvature, the initial magnetic pressure is taken into account. The magnetic pressure acts as a potential barrier and pushes the plasma outwards. As may be seen from the pressure illustration along radial axis, in figure 13. Therefore, the

initial distribution is determined to be as in the following equations, for x, y, r and z axes, accordingly.

$$f_{(x)} = |x|[1 - e^{(x^2 - a^2)}] \tag{14}$$

$$f_{(y)} = |y|[1 - e^{(y^2 - a^2)}] \tag{15}$$

$$f_{(r)} = |r|[1 - e^{(r^2 - a^2)}] \tag{16}$$

$$f_{(z)} = |z|[1 - e^{(z^2 - c^2)}] \tag{17}$$

Combining the spheroid expression given in Eq. 13 with the Eqns. 14-15-16-17, the result for x-z plane and x-y plane are given accordingly.

$$f_{y(x,z)} = a\sqrt{1 - \frac{f_x^2}{a^2} - \frac{f_z^2}{c^2}} \tag{18}$$

$$f_{z(r)} = c\sqrt{1 - \frac{f_r^2}{a^2}} \tag{19}$$

To illustrate, the resulting heat map of the particle distribution corresponding to Eqns. 19&20 at the center, on x-z plane and x-y plane are given in figure 12 with a = 2, c = 0.5 values.

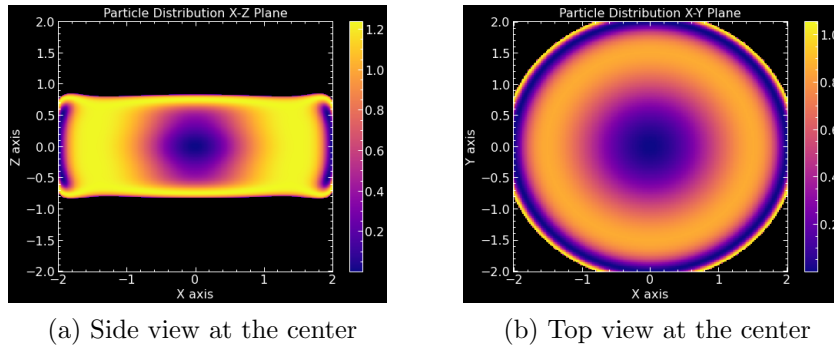(a) Side view at the center   (b) Top view at the center

Figure 12: Heatmap illustration of the particle distribution. Figure 12a represents the distribution equation of 18, along Z-X Axis, figure 12b represents the distribution equation of 19, along the radial axis.

4.4. MHD Analysis

The confinement configuration corresponds to the spherical pinch. At the center, local equilibrium corresponds to the same relation as in typical cylindrical theta pinch. In the cylindrical theta pinch, fluid velocity at equilibrium runs over azimuthal direction, and only z component of magnetic field is present. However, on the other hand, spherical theta pinch coordinates correspond to spherical symmetry rather than

cylindrical symmetry. The driven plasma current density and the magnetic field inside the configuration may be shown as,

$$\vec{J} = J_0(-\hat{\phi}) \tag{20}$$

$$\vec{B} = B_r\hat{r} + B_\theta\hat{\theta} \tag{21}$$

The magnetic force on the plasma may be expressed by Lorenz Force,

$$\vec{F} = \vec{J} \times \vec{B} = (J_0 B_\theta)\hat{r} + (J_0 B_r)(-\hat{\theta}) \tag{22}$$

Where the polar axis expansion is prevented, ensured by magnetic mirror criteria. Hence, the equilibrium is gathered ensuring that the radial fluid pressure and magnetic pressure cancel each other. The polar axis of magnetic field on the Cartesian coordinates may be found as,

$$(\vec{B})_\theta = B_0(\cos\theta\cos\phi\ \hat{x} + \cos\theta\sin\phi\ \hat{y} - \sin\theta\ \hat{z}) \tag{23}$$

On the cylindrical radial axis, x and y components vanish, since $\theta = 90°$. Hence,

$$(\vec{B})_\theta|_{\theta=90°} = -B_0\hat{z} \equiv B_z \tag{24}$$

In the theta pinch configuration, where the pressure on the RHS is expressed in Eq. 13, momentum equation on radial axis yields,

$$\left(\vec{J} \times \vec{B}\right)_r = \left(\vec{\nabla}P\right)_r \tag{25}$$

Where, by Ampere-Maxwell law, the generated current density yields,

$$J_\theta = -\frac{1}{\mu_0}\frac{dB_0}{dr} \tag{26}$$

Inputting the above expression into the momentum equation, we get the condition[20] for the equilibrium as,

$$\frac{d}{dr}\left(P_{(r)} + \frac{B_z^2}{2\mu_0}\right) = \frac{B_z}{\mu_0}\frac{dB_r}{dz}\nearrow^0 \tag{27}$$

Where the RHS of equation 29 accounts for the magnetic curvature force and negligibly small. Henceforth, the resultant pressure profile reads as,

$$P_{(r)} + \frac{B_z^2}{2\mu_0} = \frac{B_0^2}{2\mu_0} \tag{28}$$

Where $B_z \equiv Induced magnetic field$, $B_0 \equiv$ Applied magnetic field.

Now, returning back to equations 13 17, and combining them, we get the expression for the fluid pressure as,

$$P_{(r)} = P_0\left(|r|[1 - e^{(r^2-a^2)}]\right)^\gamma \tag{29}$$

Where P_0 is held unity, the final pressure profile yields as,

$$\left(|r|[1 - e^{(r^2-a^2)}]\right)^\gamma = \frac{B_0^2}{2\mu_0} - \frac{B_z^2}{2\mu_0} \tag{30}$$

Now we have the data for both fluid pressure and the applied magnetic pressure. Using both, we can determine the magnetic pressure due to the magnetic field along z direction. The magnetic field gets contributions from both the applied magnetic field and the diamagnetism behavior of the plasma, which generates magnetic field in the reverse direction. In the following figures of 13 and 14, the fluid pressure and magnetic pressure are illustrated, and the results are evaluated in the discussion.
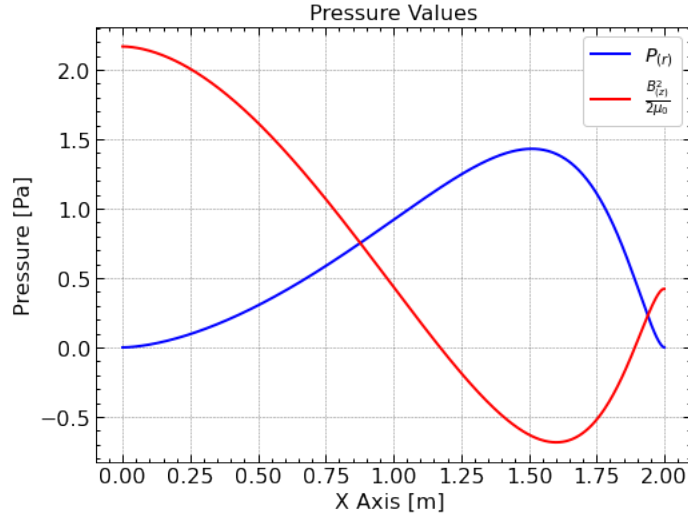

Figure 13: Showing the initially generated pressures, blue line for fluid pressure, red line for generated magnetic pressure due to diamagnetism of plasma.
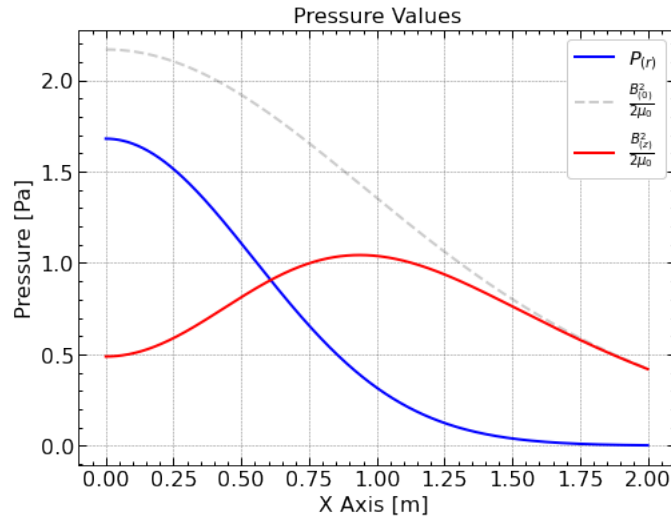

Figure 14: Showing the final generated pressures, blue line for fluid pressure, black-dashed line for pressure due to applied magnetic field, red line for the total magnetic pressure due to diamagnetism of plasma.

4.5. Discussion of MHD Equilibrium

As seen from the figure 13, magnetic pressure creates a cavity for the fluid, however, the magnetic profile given in figure 13 does not represent the equilibrium for the theta pinch, and the system is expected to evolve to a different state. The stabilized pressure profile may be seen in figure 14. Figure 14 mimics the stable theta pinch pressure configuration. The magnetic pressure created by magnetic field along z direction creates a potential barrier and reflects the fluid creating an equilibrium. Hence it may be concluded that, pressure balance occurs at this state. However, on the z-axis, due to the collisions, particles get inside the loss cone, and they get lost. To see how the system evolves, MHD simulation is required. However, for further work, the initial conditions for particle distribution is gathered as shown in the figure 12. While generating the MHD simulation, the initial mass distribution is going to be used as described by the equations 18 19.

5. Conclusion

Seeking a solution for transportation problem of mined coals, acceleration method is advised. The accelerated ions are received by a satellite that has electrostatic deceleration rings and plasma confinement machine. The deceleration component is advised to decrease the current required the hold the plasma inside the confinement machine. The necessary charge density is found in the determination of parameters section of particle deceleration simulation. With the determined charge densities, particle are successfully decelerated and transferred into spherical theta pinch (spherical magnetic mirror). In the particle confinement section, we determined the necessary conditions for ion confinement, which are the minimum current required and minimum injection angle. With the determined parameters, single particle simulation is done and seen that the ion is successfully confined within the configuration. However, single particle theory is not sufficient to determine the plasma confinement. To examine the collective behavior of plasma, MHD and Kinetic Plasma theory is used. Since S-parameter is mostly bigger than 2, it is concluded that the plasma behaves as a fluid, and formation of the plasma is not determined by the kinetic theory. Eventually, the equilibrium is tested using the equilibrium condition for theta pinch, and it is seen that the plasma is pushed towards the center, hence, radial pressure balance occurs. However, it may not be possible for the present configuration to hold the plasma in z-direction due to the collisional behavior of plasma. Therefore, as a first plasma wall, graphite may be used which also can help to cool down the plasma, or we may need to seek for another configuration method. One of which may be "Spheromak" that is proven to be successful to confine plasma.

6. Acknowledgements

the project.

7. References

[1] Miyamoto, K. (2022). Plasma Physics for Controlled Fusion (92nd ed.). Springer.

[2] Molokov, S., Moreau, R., & Moffatt, H. (2007). Magnetohydrodynamics, Historical Evolution and Trends (80th ed.). Springer.

[3] Smith, C., & Cowley, S. (2010). The path to fusion power. Philosophical Transactions Of The Royal Society A: Mathematical, Physical And Engineering Sciences, 368(1914), 1091- 1108. https://doi.org/10.1098/rsta.2009.0216

[4] National Aeronautics and Space Administration. (1988). Lunar Helium-3 and Fusion Power. In NASA Conference Publication. Cleveland. Retrieved 25 May 2022, from.

[5] Niechciał, J., Banat, P., Kempiński, W., Trybuła, Z., Chorowski, M., & Poliński, J. et al. (2020). Operational Costs of He3 Separation Using the Superfluidity of He4. Energies, 13(22), 6134. https://doi.org/10.3390/en13226134

[6] Olson, A. (2013). THE MARK IV: A SCALABLE LUNAR MINER PROTOTYPE. Madison; University of Wisconsin-Madison.

[7] Schmitt, H. (2022). Lunar Helium-3 Fusion Resource Distribution – NASA Solar System Exploration. NASA Solar System Exploration. Retrieved 25 May 2022, from https://solarsystem.nasa.gov/studies/191/lunar-helium-3-fusion-resource-distribution/.

[8] Helium-3: Lunar Gold Fever — OpenMind. OpenMind. (2022). Retrieved 25 May 2022, from https://www.bbvaopenmind.com/en/science/physics/helium-3-lunar-gold-fever/

[9] Daido, H., Nishiuchi, M., & Pirozhkov, A. (2012). Review of laser-driven ion sources and their applications. Reports On Progress In Physics, 75(5), 056401. https://doi.org/10.1088/0034-4885/75/5/056401

[10] Hinterberger, F. (n.d.). Electrostatic accelerators. https://cds.cern.ch/record/1005042/files/p95.pdf

[11] Accelerating: Radiofrequency Cavities. CERN. (n.d.). Retrieved April 20, 2022, from https://home.cern/science/engineering/accelerating-radiofrequency-cavities

[12] Savenko, N. (2006). MHD Stability and Confinement of Plasmas in a Single Mirror Cell. Uppsala Universitet.

[13] Lopes, J., & Rocha, J. (2015). Simple General Purpose Ion Beam Deceleration System Using a Single Electrode Lens. World Journal of Engineering and Technology, 03(03), 127– 133. https://doi.org/10.4236/wjet.2015.33014

[14] Rajput, J., et al. (2010). An electrostatic deceleration lens for highly charged ions. Review of Scientific Instruments, 81(4), 043301. https://doi.org/10.1063/1.3379242

[15] Chen, F. F. (2016). Introduction to Plasma Physics and Controlled Fusion. Springer International Publishing. https://doi.org/10.1007/978-3-319-22309-4

[16] Scipy.integrate.solve_ivp — SciPy v1.8.1 Manual. (2019). Scipy Manual. https://docs.scipy.org/doc/scipy/reference/generated/scipy.integrate.solve_ivp.html

[17] England, R. (1969). Error estimates for Runge-Kutta type solutions to systems of ordinary differential equations. The Computer Journal, 12(2), 166–170. https://doi.org/10.1093/comjnl/12.2.166

[18] Slough, J., & Hoffman, A. (1988). Observation of tilt stability of field reversed configurations at large s. Nuclear Fusion, 28(6), 1121–1125. https://doi.org/10.1088/0029- 5515/28/6/016

[19] Kryukov, N., Martinell, J. J., & del-Castillo-Negrete, D. (2018). Finite Larmor radius effects on weak turbulence transport. Journal of Plasma Physics, 84(3). https://doi.org/10.1017/s0022377818000351

[20] Freidberg, J. P. (2014). Ideal Mhd [E-book]. Cambridge University Press